JGR Atmospheres

RESEARCH ARTICLE
10.1029/2019JD031708

Ambient Aerosol Hygroscopic Growth From Combined Raman Lidar and HSRL

K. W. Dawson[1,2], R. A. Ferrare[2], R. H. Moore[2], M. B. Clayton[2,3], T. J. Thorsen[2], and E. W. Eloranta[4]

[1]Universities Space Research Association, Columbia, MD, USA, [2]NASA Langley Research Center, Hampton, VA, USA, [3]Science Systems and Applications, Inc., Hampton, VA, USA, [4]Space Science and Engineering Center, University of Wisconsin-Madison, Madison, WI, USA

Key Points:
- Data from combined Raman and HSRL lidars can retrieve aerosol humidification factors within the mixed layer in the Southern Great Plains
- Lidar humidification factors retrieved near the mixed layer top are comparable to surface in situ nephelometer and composition measurements
- This technique leverages the real atmospheric humidity environment to retrieve aerosol hygroscopicity over the realistic dynamic range

Supporting Information:
- Supporting Information S1

Correspondence to:
K. W. Dawson,
kyle.w.dawson@nasa.gov

Citation:
Dawson, K. W., Ferrare, R. A., Moore, R. H., Clayton, M. B., Thorsen, T. J., & Eloranta, E. W. (2020). Ambient aerosol hygroscopic growth from combined Raman lidar and HSRL. *Journal of Geophysical Research: Atmospheres*, *125*, e2019JD031708. https://doi.org/10.1029/2019JD031708

Received 23 SEP 2019
Accepted 18 MAR 2020
Accepted article online 6 APR 2020

Abstract Lidar retrievals of aerosol extinction and collocated relative humidity (RH) were acquired during the Department of Energy Combined High Spectral Resolution Lidar (HSRL) and Raman Measurement Study campaign in the summer of 2015 at the Southern Great Plains site in northern Oklahoma. Measurements of the hygroscopic properties of aerosols are crucial for accurately representing their relationship with clouds, which can be a significant source of uncertainty in assessing direct and indirect radiative effects. The ability for lidar to retrieve measurements of the vertically resolved f(RH), that is, the aerosol extinction at some wet RH normalized by the aerosol extinction at a dry reference RH, is investigated here and compared with nephelometer-measured f(RH) at the surface. We introduce a modified approach to fitting the lidar measurements of aerosol extinction and our comparisons reveal that lidar and nephelometer measurements of f(RH) are consistent, both with each other and with reported values in the literature. The implications for this work present a path forward for global-scale retrievals of remotely sensed aerosol hygroscopic properties. Most importantly, the efforts in this study could lead to closing the gap on uncertainties associated with the aerosol indirect radiative effect when combined with inversion retrievals of aerosol microphysical properties.

Plain Language Summary Atmospheric aerosols, or tiny particles suspended in the atmosphere, are an important component of the climate system. These particles can sometimes undergo humidification processes that allow them to grow in size and scatter more solar radiation. When certain conditions are met, aerosols can grow to become cloud droplets and modify cloud properties like brightness or reflectivity. Remote sensing systems can observe optical properties of aerosols on a large scale and in a timely fashion. However, some essential aspects of these aerosols, like their humidification properties, remain a challenge for remote sensing instruments to obtain. In this study, we demonstrate the capability of a unique lidar system to expand the current set of observations that are regularly retrieved by remote sensing instruments. Specifically, we make simultaneous retrievals of the atmospheric relative humidity and aerosol light extinction coefficients by combining Raman and High Spectral Resolution Lidar. We show that this system can accurately retrieve humidification properties of aerosols within the atmospheric mixed layer. These results reach a considerable milestone for the future advancement of remote sensing lidar and represent a path forward in reducing climate forcing uncertainty.

1. Introduction

Remote retrievals of aerosol properties under different humidity conditions are essential for accurately characterizing aerosol composition to better estimate aerosol impacts on climate. Aerosols perturb radiation directly by scattering and absorbing light (the direct effect) and also indirectly by modifying cloud properties through the indirect effect (e.g., Twomey, 1977). Accurately assessing aerosol humidification effects could significantly improve estimates of the first indirect effect and lead to better assessments of radiative forcing (J. Liu & Li, 2018). Aerosol humidification is complex and intimately linked with initial chemical composition and meteorological conditions and atmospheric processes like chemical aging.

Interactions among aerosols, clouds, and climate are influenced by aerosol solubility and hygroscopicity, that is, an aerosol's ability to uptake water. Hygroscopic aerosols increase in size with increasing relative humidity (RH) and that increased size scatters more solar radiation. Aerosols that modulate cloud optical

properties by seeding the formation of cloud droplets are called cloud condensation nuclei (CCN). CCN that activate to increase the number of cloud droplets will increase cloud lifetime and reflectivity (i.e., albedo) thus affecting the radiation budget. Hygroscopic aerosol has the potential to significantly modify the net amount of light scavenging of solar radiation both directly and indirectly and the relevant processes are poorly represented in models leading to large uncertainties in projections of climate change. In the past, some studies have traditionally estimated the number of these CCN using the aerosol optical depth (AOD), an optical measurement that is blind to the humidification effect. Work by J. Liu and Li (2018) estimated humidity-blind AOD as a proxy for CCN could lead to an underestimate of the first indirect effect of aerosols by up to 23%.

Aerosol hygroscopic growth is defined as the ratio of the wet particle diameter to the dry diameter. Similarly, the aerosol humidification factor $f(\mathrm{RH})$ is the ratio of the light scattering at a given RH to a reference RH typically $\leq$40% (e.g., Ferrare et al., 1998; Jefferson et al., 2017; Pahlow et al., 2006). It has also been suggested by the World Meteorological Organization to perform in situ measurements of aerosol properties between 30% and 40% RH (WMO/GAW, 2016). Several studies have examined $f(\mathrm{RH})$ both in the laboratory and in ambient in situ settings (e.g., Beaver et al., 2008; Beyersdorf et al., 2016; Crumeyrolle et al., 2014; Ziemba et al., 2013). However, scaling these laboratory studies to the real atmosphere is difficult. Ambient studies must use an auxiliary data set or model to provide the ambient RH, or alternatively, $f(\mathrm{RH})$ is estimated from parameterizing a fit to data points using in situ measurement techniques. Uncertainty arises from the latter method since various models, which are summarized in Titos et al. (2016), being used to parameterize $f(\mathrm{RH})$ can lead to different representations of the hygroscopic growth between 40% and 90% RH. Complications can arise when aerosols exhibit strong hysteresis making the selection of the correct parameterization difficult (Carrico, 2003; Kotchenruther et al., 1999). This can be especially uncertain if a small number of datapoints are used to parameterize the $f(\mathrm{RH})$ assuming a monotonic growth curve as is sometimes done for in situ aircraft measurements (Ziemba et al., 2013). Recently, Brock et al. (2016) showed that a model based on κ-Kohler theory from Petters and Kreidenweis (2007) represented the submicron aerosol hygroscopic growth in the southeastern United States better than the commonly used gamma power law approximation (Hänel, 1972). Identifying which parameterization is appropriate shows the need for determining aerosol properties along the RH continuum and in different source regions.

The Department of Energy Atmospheric Radiation Measurement (ARM) program sought to explore the evolving aerosol measurement capabilities of lidar during the.

Combined High Spectral Resolution Lidar (HSRL) And Raman lidar Measurement Study (CHARMS). During CHARMS, aerosol optical properties and RH were measured simultaneously at the Southern Great Plains (SGP) central facility via a so-called $3\beta + 2\alpha$ lidar instrument configuration. Aerosol backscatter profiles were measured at three wavelengths (i.e., 3β) and aerosol extinction profiles were measured at two wavelengths (i.e., 2α). In this study, increased light extinction by aerosols was observed within well-mixed boundary layers that were identified by remotely sensed temperature and water vapor profile gradients. Nearly constant thermodynamic gradients help to isolate changes in light extinction due primarily to changes in RH rather than aerosol mass. We provide a data set for vertically resolved aerosol properties as a function of simultaneously retrieved ambient RH and showcase the evolution of lidar capability toward observations of aerosol hygroscopic growth in the ambient environment with added capability of retrievals of aerosol volume. Furthermore, we show that advantages in multiwavelength lidar retrievals of $f(\mathrm{RH})$ are twofold: (1) Given that meteorological conditions are satisfied, the lidar acquires profiles of aerosol humidification every 10 min compared to the 1-hr RH and cutoff size-dependent duty cycle of the nephelometers at SGP and (2) retrievals of vertically resolved $f(\mathrm{RH})$ at or near cloud base are relevant for the aerosol microphysical and chemical properties directly influencing cloud formation and indirect radiative forcing. The results in this work demonstrate these advantages and provide a pathway to constrain models by the ability to characterize aerosol properties with RH under a wide range of ambient meteorological conditions.

Section 2 introduces a method for parameterizing the $f(\mathrm{RH})$ retrieved by the lidar system, nephelometers, and other ARM surface instruments. In section 3 we present a model for estimating the $f(\mathrm{RH})$ from ARM measurements of surface-chemistry and ambient column size distributions. Next, in section 4, we examine the bulk and temporally variable $f(\mathrm{RH})$ for the CHARMS campaign at SGP along with other relevant lidar parameters. We show the comparison of the lidar-retrieved and nephelometer-measured $f(\mathrm{RH})$ to the

model-derived f(RH) that assumes surface aerosol chemical composition. These methods and their implications for retrieving the f(RH) are then discussed.

2. Methods

2.1. The Combined HSRL and Raman Lidar Measurement Study (CHARMS)

CHARMS occurred at the Department of Energy ARM SGP facility from July through September 2015 and acquired coincident lidar retrievals of vertically resolved aerosol properties and RH. The ARM Raman lidar (Goldsmith et al., 1998) measured profiles of aerosol backscatter (β) and extinction (α) coefficients at 355 nm and water vapor mixing ratio (r). The University of Wisconsin HSRL (Grund & Eloranta, 1991) simultaneously measured profiles of β, α, and depolarization ratio (δ) at 532 nm and β at 1,064 nm. RH profiles were computed from the Raman lidar r profiles (Turner et al., 2002; Whiteman et al., 1992) and the colocated Atmospheric Emitted Radiance Interferometer (AERI) temperature profiles (Feltz et al., 2003). The ARM SGP site (Sisterson et al., 2016) also had a number of ground-based instruments that measured aerosol properties in situ including a humidity-scanning nephelometer at three wavelengths (Anderson et al., 1996; Jefferson et al., 2017), an aerosol chemical speciation monitor (ACSM) (Parworth et al., 2015), and an Aerosol Robotic Network (AERONET) Sun photometer (Holben et al., 1998). Raman lidar and HSRL aerosol backscatter and extinction coefficient profiles and cloud detection were processed following Thorsen et al. (2015) and Thorsen and Fu (2015). Cloud base heights were obtained from the ARM ceilometer. Aerosol microphysical properties (e.g., aerosol volume) were preliminarily retrieved by optimal estimation inversion of the $3\beta + 2\alpha$ setup. Work assessing the optimal estimation retrievals is currently in progress and is the subject of another paper; however, inclusion of the preliminary results facilitates discussion for future lidar systems.

SGP is a rural site with local land use dominated by farming. The nearest major urban sources are over 100 km away to the north and south (Parworth et al., 2015). Wind speed and direction were measured by stationary, up-looking Doppler lidar (Newsom, 2012; Pearson et al., 2009). The mean wind during CHARMS was southerly ($\theta = 179° \pm 32°$) at 8.5 ± 4.0 m/s (1 standard deviation), consistent with the climatology from Parworth et al. (2015). Evidence from HYSPLIT back trajectory analyses shows little divergence of the plume wind history for the 72 hr before midnight on 4 August (supporting information Figure S2). Influences from advection of multiple aerosol sources are unlikely to be a factor for the data examined in this study.

2.2. Layer Selection Criteria for f(RH) Retrievals

While laboratory experiments can benefit from controlled RH and particle conditions, ambient remote sensing measurements have to deal with changing meteorological and aerosol conditions. Variable aerosol loading, composition, and state conditions can make effects from hygroscopic growth ambiguous to observe in nature. Fortunately, CHARMS allowed simultaneous profiling of meteorological and aerosol parameters that defined the state of the convective boundary layer (CBL).

Profiles of virtual potential temperature (θ_v) from the AERI and Raman lidar r were used to characterize the homogeneity of the CBL. The data set was restricted to daytime retrievals with heights >800 m above ground level to be outside of the lidar overlap region. The top of the CBL (z_i) was estimated from wavelet covariance of the aerosol backscatter coefficient (β) at 532 nm and is termed the mixed layer height (MLH) (Davis et al., 2000; Pal et al., 2010).

Derivatives in aerosol properties were used to identify potential layers meeting conditions for retrievals of f(RH). The aerosol property derivatives used for layer detection were per fractional RH ($\partial/\partial \mathrm{RH_f}$) for monotonically increasing aerosol extinction coefficient (α) and β, extinction to backscatter ratio, hereafter called the lidar ratio (S_p), and monotonically decreasing depolarization ratio (δ). This selection method prevents biasing hygroscopic growth on the lower or upper (i.e., deliquescent or efflorescent) branches of the humidogram. Ferrare et al. (1998) showed that the ratio of aerosol extinction-to-backscatter (i.e., the lidar ratio) increases with RH up to ~90%; thus, $\partial \mathrm{S_p}/\partial \mathrm{RH_f} > 0$. The aerosol depolarization ratio is correlated to particle hygroscopicity as it is inversely proportional to particle sphericity. Assuming a uniform refractive index, humidified aerosol particles are thought to be more spherical from condensing water vapor and surface tension resulting in lowered depolarization ratio such that $\partial \delta/\partial \mathrm{RH_f} < 0$ (Cooper et al., 1974).

Once potential aerosol layers have been identified by the aforementioned derivatives, additional checks are made to ensure the likelihood of a well-mixed boundary layer. The virtual potential temperature θ_v and r are good indicators of a well-mixed boundary layer (Feingold, 2003; Granados-Muñoz et al., 2015; Pahlow et al., 2006). Ambient temperature should decrease with height such that θ_v is nearly constant with respect to altitude where we set a threshold for bins not to exceed ±10 K/km based on Table 1 in Lv et al. (2017). Also following Lv et al. (2017), profiles are inspected for nearly constant r with respect to altitude to be <9 $g{\cdot}kg^{-1}{\cdot}km^{-1}$. The resulting median profiles (with interquartile ranges) are shown in supporting information Figure S1. The number of 10-min lidar profiles passing layer selection was $N = 874$ (774 cloud-free) out of 1,503 (58%) daytime profiles. The layer conditions (shown in Figure S1a–S1c) resemble other studies quantifying lidar retrieved ambient aerosol humidification (Bedoya-Velásquez et al., 2018; Granados-Muñoz et al., 2015; Lv et al., 2017).

2.3. Humidogram Parameterizations

Given constant aerosol number density, the growth in aerosol size due to humidification effects was first related to the change in aerosol scattering coefficient by Kasten (1969). The ratio of wet to dry aerosol size was shown to be related to the ratio of the aerosol scattering coefficients by the single-parameter gamma parameterization first introduced by Hänel (1972). The gamma (γ) parameterization for the enhancement in light scattering f(RH) is shown in equation 1 (Zieger et al., 2011).

$$f(RH) \cong \frac{\alpha}{\alpha_0} = C_1(1-\mathrm{RH_f})^{-\gamma} \tag{1}$$

In equation 1, C_1 is a second parameter substituted with the expression where there is no scattering enhancement at some reference RH so that $C_1 = (1 - \mathrm{RH_{f,0}})^{\gamma}$. We assume that aerosol absorption is not dependent on RH so that f(RH) from here on refers to enhancement of aerosol extinction due to increased scattering. Aerosol absorption was measured at RH < 40% by the three-wavelength ARM Particle Soot Absorption Photometer and was added to the nephelometer scattering measurements to produce aerosol extinction. Here we set $\mathrm{RH_{f,0}} = 0.40$.

Brock et al. (2016) proposed another parameterization for f(RH) with the same functional form as in Hänel (1968) with an extinction equivalent hygroscopicity parameter (κ_{ext}). We use the equation from Brock et al. (2016) as a second parameterization to our retrievals of f(RH) as shown in equation 2, with the modification of the parameter C_2 serving the same function as C_1. Particles often do not show enhancement in aerosol extinction below RH = 40%. Incorporating C_1 and C_2 helps to standardize the retrievals of the fit coefficients across profiles by normalizing all growth curves to be 1 at RH = 40%, even when there are no available retrievals at ambient RH = 40%. At a reference RH of 40%, $C_2 = [1+0.67\kappa_{ext}]^{-1}$. We restrict our data to aerosol with depolarization ratios <20% to avoid uncertainties in Mie scattering from aspherical particles like dust.

$$f(RH) = \frac{\alpha}{\alpha_0} = C_2\left[1 + \kappa_{ext}\left(\frac{RH_f}{1 - RH_f}\right)\right] \tag{2}$$

In this work, we ascertain best fit coefficients for each lidar profile using a matrix approach that smoothes the parameterizations from equations 1 and 2 over three lidar profiles. We apply a least squares fitting approach over 30 min to be consistent with nephelometer RH scan times. Equations 1 and 2 are combined requiring the same fit coefficient estimate per profile of α_0 and the same fit coefficient estimates for γ and κ_{ext} across all profiles. We make a notation substitution for clarity where F_1(RH) is the bracketed term in equation 1 and F_2(RH) is the bracketed term in equation 2. We define column vectors of the extinction coefficient at ambient RH and reference RH as $\vec{\alpha} = [\alpha_{k-1}; \alpha_k; \alpha_{k+1}]$ and $\vec{\alpha}_0 = [\alpha_{0,k-1}; \alpha_{0,k}; \alpha_{0,k+1}]$ for the lidar profiles $k - 1$ to $k + 1$. Next, we define the column vectors of the functional parameterizations in equations 1 and 2 as

$$\vec{f}_1 = C_1[F_1(\mathrm{RH_{k-1}}); F_1(\mathrm{RH_k}); F_1(\mathrm{RH_{k+1}})]$$

and

$$\overrightarrow{f}_2 = C_2[F_2(\mathrm{RH_{k-1}}); F_2(\mathrm{RH_k}); F_2(\mathrm{RH_{k+1}})]$$

The coefficients C_1 and C_2 are the same as in equations 1 and 2. We multiply the vectors $\vec{\alpha}$ and $\vec{\alpha}_0$ by the matrix $\boldsymbol{L_I}$ defined as $\boldsymbol{L_I} := [\boldsymbol{I}_3, \boldsymbol{I}_3]^T \in \mathbb{R}^{6\times 3}$, where $\boldsymbol{I}_3$ is the identity matrix of dimension 3. The resulting combined fit equation is shown in equation 3. The product on the right-hand side of equation 3 is the Hadamard (elementwise) product.

$$\boldsymbol{L_I}\vec{\alpha} = \boldsymbol{L_I}\vec{\alpha}_0 \circ \begin{bmatrix} \overrightarrow{f}_1 \\ \overrightarrow{f}_2 \end{bmatrix} \tag{3}$$

Spherical particles (i.e., nondust) with diameters <1 μm have been shown to contribute ~78% of the aerosol extinction at 530 nm and are in the range where $Q_{\mathrm{ext}} \propto r_{\mathrm{p}}$ for typical size distributions derived from sun photometer measurements (Brock et al., 2016; Ferrare et al., 1998). The aerosol backscatter efficiency for small scattering angles, however, is highly nonlinear in this size range so we do not parameterize the aerosol backscatter humidification factor f_β (RH).

2.4. Uncertainty in f (RH) Retrievals

Uncertainties in lidar measurements of extinction are assumed to be less than ~20% at 532 nm (Burton et al., 2016). The Raman-retrieved RH is estimated to be retrieved to an accuracy of 5–20% depending on temperature retrieval quality (Mattis et al., 2002). Assuming 20% error in humid and dry extinction coefficient retrievals and 20% error in RH and adding in quadrature yields an expected error in f (RH) at 532 nm of ≤35% with maximum errors contained within the CBL. High accuracy temperature measurements will significantly constrain errors to <35%. For this study, the collocated AERI at SGP was used for temperature retrievals to overcome Raman lidar limitations from incomplete overlap near the surface. Later, we compare results of f (RH) at 355 and 532 nm. For these comparisons, the random uncertainty of the Raman 355-nm extinction retrievals was available and is used to provide error estimates on the retrieval quality at 355 nm. However, error information for the 532-nm retrievals from the University of Wisconsin lidar was not available and the calculation of it required efforts beyond the scope of this paper (e.g., see Z. Liu et al., 2006). Instead, we apply a constant relative uncertainty in aerosol extinction coefficient of 20% at 532 nm. Because the f (RH) retrievals are calculated at RH = 85% and the relative error in the Raman + AERI retrieved RH is taken to be <10%, we can approximate the error in f (RH) at an RH = 85% to be well captured by the error in the retrieved extinction coefficient (see supporting information). Recalling that the f(RH) is the ratio of the extinction coefficient (at RH = 85%) normalized by a fit coefficient of extinction coefficient (at RH = 40%), the uncertainty in f(RH) is just due to the uncertainty of the RH-dependent extinction coefficient, where the uncertainty in the fit coefficient is not considered. Thus, the absolute error in f (RH) at 532 nm is just $\delta(f_{RH}) = 0.2f(RH)$. See the supporting information Text S1 and Figure S4 for more details on calculating uncertainties.

3. Modeling f (RH) With Available ARM Measurements

3.1. Estimating κ From Chemical Composition

The ARM suite at SGP has surface measurements of aerosol composition from the ACSM. Nonrefractory, fine mode composition at SGP in summertime was mainly composed of organics and sulfate (e.g., see Figure S3a). Six days of useable ACSM data were available during CHARMS. The mean mass loading over those six days was 9 μg/m^3 with an organic and sulfate mass fraction of 66% and 26%, respectively. The distribution of the surface mass fractions remained relatively constant with the largest standard deviation equal to 12.5% for the organic aerosol component. Inorganic aerosol hygroscopicity and volume were calculated using the Extended Aerosol Inorganic Model (E-AIM) with variable RH (Clegg et al., 1998). The model inputs were RH and four inorganic species from the ACSM. Hydronium ions were added when necessary to achieve ion balance. Cases where cations exceeded anions were rare and not analyzed. The model outputs were the inorganic hygroscopicity parameter and the inorganic volume of aqueous phase compounds. The bulk hygroscopicity parameter, including organics with an assumed density of 1.4 g/cm^3 and hygroscopicity of 0.15, is calculated using the Zdanovskii–Stokes–Robinson (ZSR) volume fraction mixing rule (Petters &

Kreidenweis, 2007). The assumed organic aerosol density is typical of secondary organic aerosol (Kostenidou et al., 2007), while the assumed organic aerosol hygroscopicity is typical of aerosol at ARM SGP with south-easterly influence (Gasparini et al., 2006). The bulk hygroscopicity parameter is converted to growth factor following equation 4 where fractional RH is assumed approximately equal to water activity for the humidity ranges relevant in this study.

$$g_v(RH) \equiv \frac{V}{V_0} \cong 1 + \kappa \frac{RH_f}{(1 - RH_f)} \tag{4}$$

In equation 4, V is the aerosol volume, V_0 is the dry aerosol volume, RH_f is fractional RH, and κ is the aerosol hygroscopicity parameter.

3.2. Aerosol Microphysical Properties

The ARM SGP site did not have measurements of surface aerosol dry size distributions available due to instrument failures during CHARMS. However, the AERONET Sun photometer measured solar and sky radiances that were used to retrieve ambient columnar aerosol size distribution and complex refractive index (m). We make use of these retrievals since the modeled estimates of f(RH) require input of an RH-dependent aerosol size distribution. We assume that the AERONET retrievals are dominated by aerosols in the CBL because the CBL contains most of the AOD (i.e., integrated extinction coefficient). This assumption applies to modeled estimates of the f(RH) for 2 days of this analysis shown in section 4.2. We check the validity of the assumption by comparing the AERONET AOD with the HSRL AOD within the mixed layer and as a total column for the coincident time. Our comparison showed 80% of the AOD to be within the altitude range between the lidar overlap region and 3,000-m height. Additionally, the HSRL-integrated extinction coefficient resulted in an AOD of 0.19 for the total column, matching the AERONET value with error ~1%. We additionally assume that the AERONET columnar volume size distribution and m are representative for an extinction-weighted average RH, measured by the lidar, because AERONET makes retrievals under ambient conditions. Lastly, all aerosol particles in the volume size distribution are assumed to be compositionally size-independent and the E-AIM estimated growth factor is multiplied on the entirety of the size distribution.

The real and imaginary parts of the complex refractive index m as a function of the RH is modeled by equation 5 (Hänel, 1976; Levoni et al., 1997).

$$m(RH) = m_w + (m_0 - m_w) g_v(RH)^{-1} \tag{5}$$

In equation 5, m_w is the refractive index for water and is 1.33, m_0 is the dry refractive index and g_v is the volume growth factor as in equation 4. An example of model inputs and outputs from 2 August 2015 is shown in Figure S3. The modeled AOD is calculated using Mie theory from Bohren and Huffman (1998) with an RH-dependent size distribution weighted by the lidar-sensitive region from Ferrare et al. (1998) and shown in Figure S3d. Contributions of the coarse mode of the size distribution can significantly increase the result of the modeled f(RH) (Zieger et al., 2014, 2013). This is accounted for by weighting the extinction efficiency by the lidar-effective range from Ferrare et al. (1998) and shown by the gray shaded region in Figure S3d. The resulting columnar f (RH) is then the AOD at RH = 85% normalized by the AOD at RH = 40% and is compared with nephelometer measurements. Because the dry RH inside the nephelometer varies, the f(RH) from the nephelometers were forced to be 1 at RH = 40% by fitting the data with equation 2. The mean ± 1 standard deviation of the nephelometer dry RH was 38.9% ± 6.5%. The fine mode aerosol chemical composition and the weighting of the size distribution from the lidar sensitive region make the modeled f(RH) comparable to the nephelometer PM_1 retrievals.

4. Results

4.1. Lidar Parameters as a Function of RH

The lidar extinction coefficient from all useable profiles during the 2-month-long CHARMS campaign is presented in Figure 1 as a function of retrieved RH. Figure 1 shows the median of the extinction coefficient with the interquartile range. These data are for cloud-free profiles that satisfy the conditions described in section 2.2. The expected monotonic behavior of aerosol extinction with increasing RH is exhibited in the CHARMS

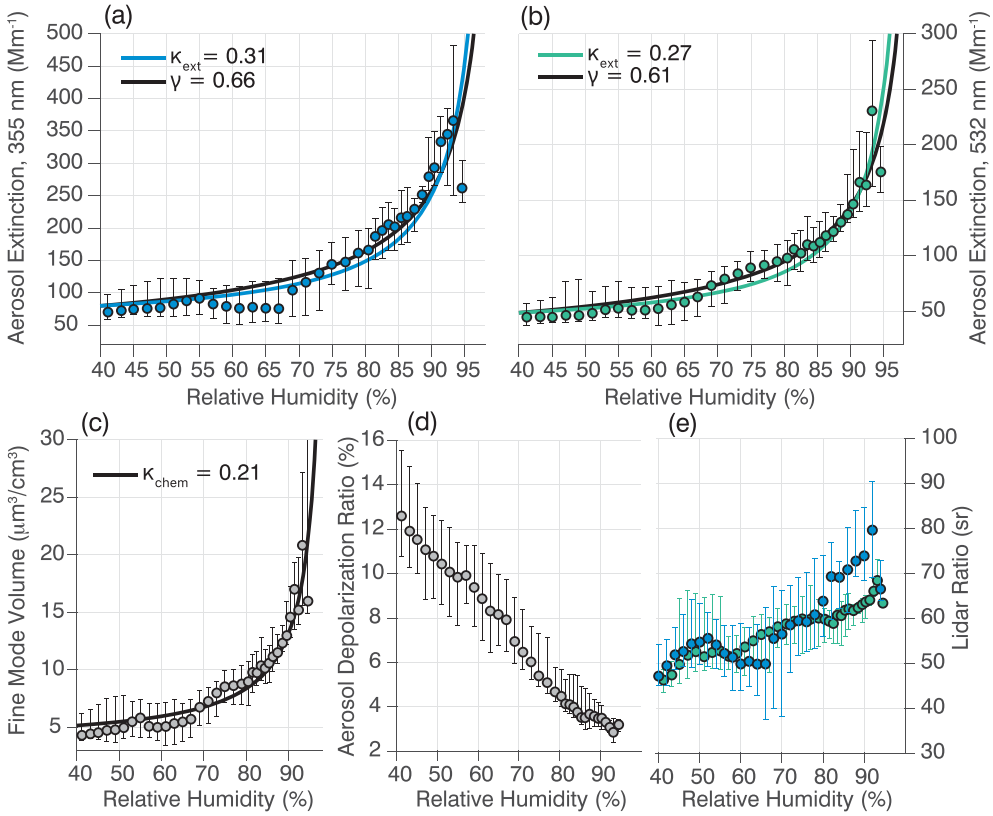

Figure 1. Humidograms of aerosol extinction at (a) 355 nm and (b) 532 nm binned by lidar-AERI retrieved RH, (c) aerosol fine mode volume, (d) 532-nm depolarization ratio, and (e) 355-nm (blue) and 532-nm (green) lidar ratio. Medians are filled circles, and interquartile ranges are error bars. Lines for f (RH) and g_v (RH) are overlaid in panels (a and b) and (c), respectively. The kappa (gamma) fit is shown in (a) and (b) where $\kappa_{ext} = 0.31$ and 0.27 ($\gamma = 0.66$ and 0.61) for 355 and 532 nm, respectively. The aerosol extinction coefficient at reference RH = 40% is $\alpha_0 = 79.8$ and 48.7 Mm^{-1} for 355 (blue) and 532 (green) nm, respectively. The aerosol volume at RH = 40% is 5.2 $\mu m^3/cm^3$ with $\kappa_{chem} = 0.21$.

data set for both wavelengths in Figures 1a and 1b. The corresponding lidar observables shown in Figures 1c–1eshow this expected behavior as well, confirming the effectiveness of the layer selection methods in section 2.2. Although the fine mode volume concentration in Figure 1c is a preliminary inversion product derived by optimal estimation, the increasing behavior with RH is consistent with aerosol growth factors retrieved from in situ instruments. The depolarization ratio in Figure 1d decreases as aerosol particles become more spherical from the condensation of water vapor at higher humidity. In Figure 1e, the lidar ratio shows an increasing trend with RH similar to that shown in Ferrare et al. (1998). The same trend is observed for the 355-nm lidar ratio. The increasing lidar ratio with RH for the aerosol during CHARMS agrees well with the model results for continental aerosols presented in Figure 3 of Ackermann (1998). This result demonstrates the potential bias in aerosol extinction coefficients retrieved by multiplying aerosol backscatter coefficients with a constant lidar ratio as is done for elastic backscatter like Cloud-Aerosol Lidar with Orthogonal Polarization.

The f (RH) parameters fitted to the bulk data set can provide a rough characterization for summertime aerosol hygroscopic growth in northern Oklahoma. For CHARMS, the median retrieved κ_{ext} (γ) was 0.31 (0.66) and 0.27 (0.61) for 355 and 532 nm, respectively (Figures 1a and 1b). Values retrieved for γ are similar to those from the recent study by Chen et al. (2019). Interestingly, the composition from the ACSM during CHARMS (see supporting information) indicated a likely presence of weak organic acids as compared to the more acidic aerosol in Chen et al. (2019). We suspect drivers influencing the hygroscopicity beyond acidity, like solubility, are likely at play at SGP. The root-mean-square error (RMSE) of the parameterization to the medians was 35.3 (29.4) Mm^{-1} and 14 (11.4) Mm^{-1} for 355 (and 532) nm. Comparing the parameterizations to data within the interquartile range gives an RMSE of 52 (25.5) Mm^{-1} for 355 (and 532) nm. It should

be noted that there is uncertainty in the retrievals of the RH so that some of the variability shown in Figures 1a and 1b is due to inaccuracies in RH. This statistical plot can overcome those random errors, but per profile retrievals should focus on highly accurate retrievals of RH. The multispectral setup of this $3\beta + 2\alpha$ system provides additional insight into the f(RH) retrievals since the 355-nm wavelength is sensitive to smaller aerosols than the 532-nm wavelength (e.g., Ferrare et al., 1998, their Figure 3). Larger fit coefficients for aerosol extinction at 355 nm (Figure 1a) compared to 532 nm (Figure 1b) indicate slightly more hygroscopic aerosols present at smaller size ranges. As Figure 1 is a campaign-averaged comparison and the difference between κ_{ext} at 355 nm compared to 532 nm is small, we take a closer look at these findings in section 4.2. Future lidar advancements show promise in inversion retrievals of the aerosol volume concentration. Preliminary analyses have been conducted here in Figure 1c and show the model fit from equation 4 with an RMSE of 1.3 $\mu m^3/cm^3$. These data products will be exceptionally important for future studies as a spectral dependence of optical f (RH) could convolute hygroscopicity estimates for climate modeling applications.

4.2. Case Studies of Single Profiles of f (RH)

The 10-min CHARMS profiles can be used to examine the evolution of f(RH) and the impact of cloudy or hazy conditions provided that mixed boundary layer conditions are met. During the 2-month campaign, 2 and 3 August had the longest periods of favorable mixed layer characteristics for investigating f (RH). Another advantage during these days was the availability of SGP ARM ground instrumentation for comparison and auxiliary measurements. Figure 2 shows the timeseries of the analysis region on 2 August (left column) and 3 August (right column) with the corresponding nephelometer retrievals at the ground for PM_1 and PM_{10} along with model results. Aerosol extinction coefficient is shown in Figures 2a1 and 2a2 immediately following cloudy conditions as determined by ARM ceilometer retrievals. The middle row shows combined Raman-AERI retrieved RH. There is a region of high RH at the top of the mixed layer on 2 August. The high-humidity layer was below the MLH as detected by aerosol backscatter retrievals and is not analyzed. AERI retrievals of temperature at the MLH can be subject to increased uncertainties above 0.9 MLH as compared to collocated sounding measurements (supporting information Text S2 and Figure S5). Additionally, Rauber et al. (2013) showed that clouds can affect the surrounding environment and aerosol properties by horizontally entraining cloudy air at the boundaries up to ~2 km. This dynamic region, however, is not conducive for analysis of aerosol properties that rely on constant chemical composition and concentration/size distribution; thus, the humidity region with RH > 85% in Figure 2 b1 is not analyzed.

Figure 2c1 shows that the lidar-retrieved $f(RH_{85})$ at RH = 85% is often comparable to corresponding nephelometer ground measurements whereas there are differences on 3 August (Figure 2c2). Note that comparisons between lidar and nephelometer were done after adjusting nephelometer measurements to 532 nm via the Angstrom exponent relationship between the nephelometer blue (450 nm) and green (550 nm) wavelengths. An advantage in the lidar retrievals is the ability to acquire data at a higher time resolution and closer to cloud base as compared to the 30-min duty cycle of the nephelometer. The comparison in Figures 2c1 and 2c2 shows more variability in the lidar retrieval with respect to the nephelometer allowing the lidar to capture the enhancement in the humidification factor between 21:30 and 22:30 UTC.

The nephelometer suggests the presence of a less hygroscopic coarse mode evidenced by the lower $f(RH_{85})$ for PM_{10} and in agreement with the lidar retrievals in Figures 1a and 1b. This cannot be easily confirmed without some unavailable auxiliary information of chemical composition and particle size distribution. To estimate these impacts, however, we use the fine mode (particle diameter < 1 μm) ARM ACSM ground-level aerosol chemical composition, with size distribution measurements at SGP retrieved from the closest AERONET retrieval to estimate the impact of fine mode aerosol chemistry on f(RH). The modeling framework as described in section 3.2 was implemented using AERONET column size distribution, the ARM ACSM submicron ion composition measurements, and the E-AIM thermodynamic equilibrium model. The ground-based nephelometer measurement of the aerosol extinction f(RH) represents the value for surface layer aerosol size distribution and chemical composition. The lidar retrieval represents the value for aerosol characteristics near the MLH. We use the modeling framework as a representation of the column f(RH) for fine mode aerosols, assuming surface-level aerosol chemical composition in an effort to resolve some differences in the two optical retrievals.

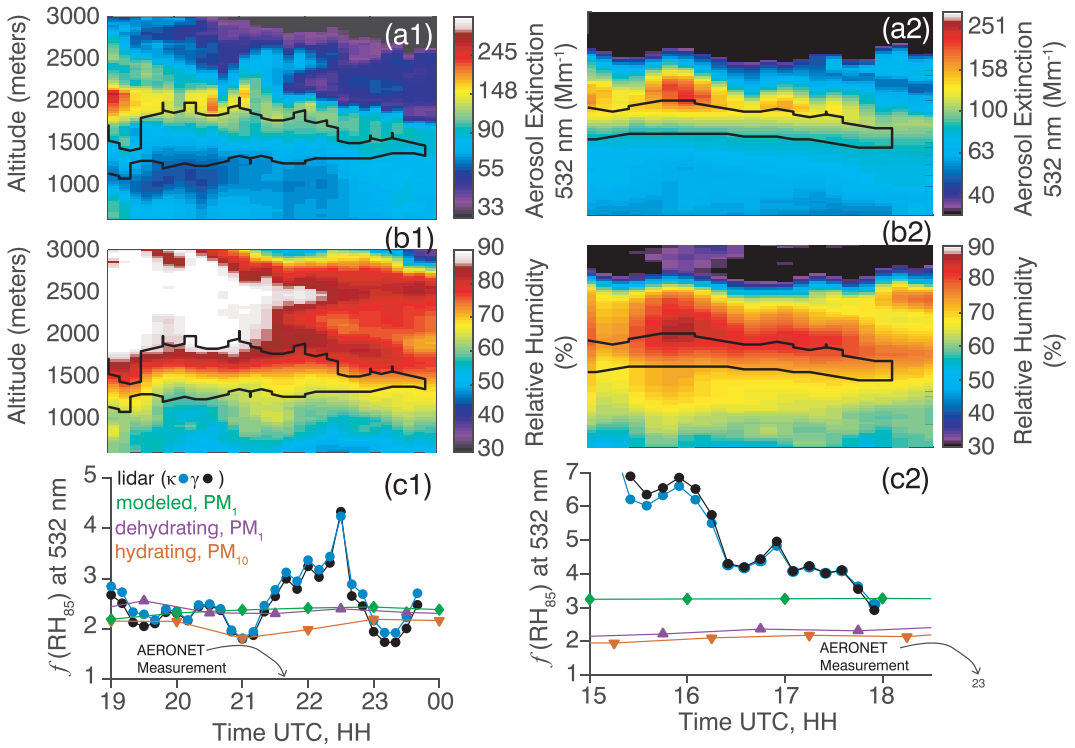

Figure 2. (a1, a2) Aerosol extinction coefficient from HSRL lidar at 532 nm. Black contours outline the region used for retrieving f(RH) and correspond to the filter criteria in section 2.2. (b1, b2) Retrieved RH from Raman water vapor mixing ratio and collocated AERI temperature retrievals. (c1, c2) Humidification factor at 85:40% RH. Lidar retrievals are for both the kappa (blue circles) and gamma (black circles) parameterizations. Nephelometer retrievals use the kappa parameterization and are for PM_{10} cutsize (orange inverted triangles) and PM_1 cutsize (purple triangles) branches of the humidogram. The modeled f(RH) using the hourly ACSM chemistry and nearest AERONET size distribution at the UTC time 21:38 (hh:mm) and 22:59 (hh:mm) on 2 and 3 August, respectively, is also pictured (green diamonds). The left column is for 2 August 2015, and the right column is for 3 August 2015.

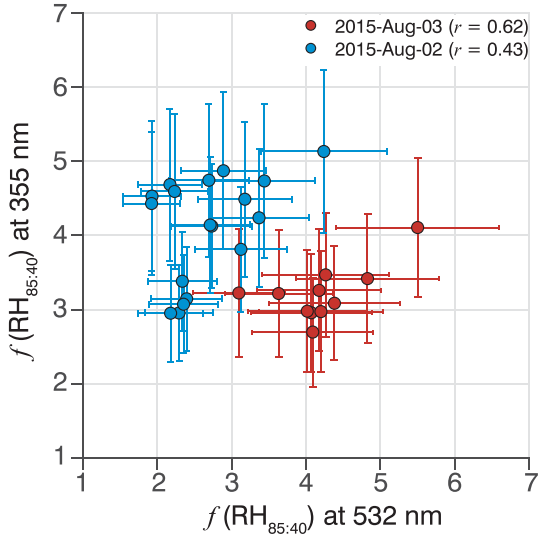

Figure 3. Comparison of f(RH) at 85% RH with uncertainty estimates for 2 August (blue) and 3 August (red).

Hourly submicron aerosol chemistry from the ARM ACSM on 2 August (and 3 August) and the AERONET size distribution retrieval at 21:38 (22:59) UTC produce the green line in the lower panel of Figure 2. In general, the modeled PM_1 f(RH_{85}) compares well to the nephelometer PM_1 branch in Figure 2c1 suggesting that the surface aerosol chemistry using column size distribution does not explain the enhancement observed by the lidar. Interestingly, using the AERONET size distribution on 3 August helps to increase the modeled f(RH) closer to values that were retrieved suggesting the column size distribution to be more representative of the near-cloud retrieval for this case. This result further illustrates the importance of making retrievals of f(RH) near cloud base or the MLH. The very large values for f(RH) that were retrieved in Figure 2c2 may be artifacts of the retrieval but the result decreases with time to match the modeled values suggesting some skill. The reason for the suspect high values may highlight a difficulty in identifying boundaries between cloud and aerosol using remote sensing.

4.3. Uncertainties in Single-Profile Lidar Retrievals of f(RH)

As mentioned in section 2.4, we can get an estimate on the absolute uncertainty in the lidar retrievals of f(RH). It is advantageous to use the reported random uncertainty in the aerosol extinction coefficient at RH = 85% since above 85%, the uncertainty in the RH retrieval can

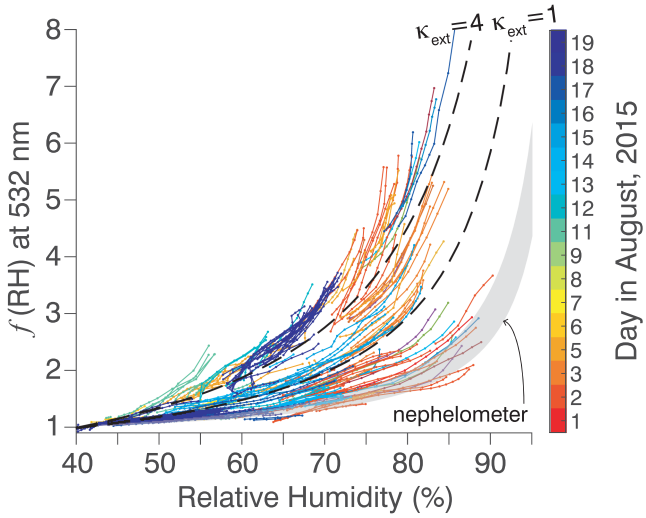

Figure 4. CHARMS lidar profiles during August, converted to f (RH) at 532 nm with the range of nephelometer retrievals in gray shading. The boundaries where $\kappa_{ext} = 1$ and $\kappa_{ext} = 4$ are shown by the dashed black lines.

rapidly dominate the retrieval in the extinction coefficient. In Figure 3 we compared the lidar retrieved values of $f(RH_{85:40})$ and calculated the absolute uncertainty as $\delta(f_{RH}) = f(RH)\frac{\delta\alpha}{\alpha}$ where $\delta\alpha$ is reported in the Raman lidar data product. This estimate of uncertainty assumes no error in the normalization constant, that is, α at 40% RH. Figure 3 shows the comparison of $f(RH_{85:40})$ for the same 2 days in Figure 2.

Recall the nephelometer PM_{10} shows a lower hygroscopicity compared to the PM_1 for both days, although the difference is more pronounced on 2 August. The multispectral lidar setup in this work, as mentioned in section 4.1, may contain information on aerosol size and corresponding hygroscopicity based on the resulting comparisons of f(RH) at two wavelengths. Lidar comparisons on 2 August of $f(RH_{85})$ at 532 and 355 nm reveal larger $f(RH_{85})$ at 355 nm with an $r = 0.43$ for the data shown in Figure 3. On average, $f(RH_{85})$ at 355 nm was 58% ± 38% (1 standard deviation) larger than the $f(RH_{85})$ at 532 nm suggesting more hygroscopic aerosol at smaller sizes, in agreement with the pictured nephelometer results on Figure 2c1. However, the same comparison on 3 August shows f (RH) to be 22% ± 11% larger at 532 nm than at 355 nm with $r = 0.62$, opposite to and less than that observed on 2 August. When we compare the difference in f (RH) between 355 and 532 nm as a function of RH over all available data during CHARMS (see supporting information Text S3 and Figure S6), we find that f (RH) at 355 nm is generally smaller than f (RH) at 532 nm. Similarly, f (RH) at 355 nm often correlates to f (RH) at 532 nm, with minimum correlation coefficients between 60% and 70% RH. Drawing any further conclusions on this trend is difficult due to the lack of control on constant size distribution and chemical composition over the limited data available during the CHARMS campaign.

4.4. Limitations of Lidar-Retrieved f (RH)

The nephelometer measurements of f (RH) during CHARMS were generally stable with little variability. Figure 4 shows that the lidar retrievals, on the other hand, had both comparable and enhanced, likely unphysical, hygroscopicity values as compared to the nephelometer. Specifically, the boundary $f(RH_{85}) = 4$ (or $\kappa_{ext} = 1$) revealed that lidar retrievals of humidification factor are subject to uncertainty despite mixed layer criteria being satisfied. There are high hygroscopicity profiles that emerge for some of the days during the campaign. These profiles have κ_{ext} values >1 and are likely contaminated by changing aerosol concentration and/or chemical composition. A few profiles even showed hygroscopicity retrievals with $\kappa_{ext} > 4$. The analysis from Zieger et al. (2011) compared the f (RH) from nephelometer measurements in the Netherlands from a variety of aerosol sources and found $f(RH_{85})$ to always be <~4. Results of $f(RH_{85}) > 4$ at 532 nm when analyzing retrievals of the humidification factor from lidar should probably be filtered out. A record of retrievals of f (RH) at various ground sites across the globe is available from Burgos et al. (2019). Future comparisons of lidar-retrieved and Burgos et al. f (RH) with corresponding in situ measurements of composition and particle size distribution would be especially illuminating for drawing statistical relationships on spectral and physicochemical variability.

5. Conclusions

In this paper, we have shown retrievals of extinction f (RH) at 355 and 532 nm from a combined Raman lidar-HSRL systems implemented during the summertime CHARMS campaign at the SGP site in northern Oklahoma. The unique ability of this $3\beta + 2\alpha$ system to retrieve aerosol properties as a function of simultaneously retrieved RH was due to the remotely sensed profiles of water vapor mixing ratio and temperature provided by the Raman lidar and AERI interferometer, respectively. The effects of humidification on the aerosol population cannot be determined unless the aerosol composition and concentration are constant with time within the vertical profile. The Raman lidar and AERI interferometer were used to identify layers contained in the boundary layer that were well mixed and within a neutrally stable regime. Although the ambient atmosphere is dynamic, some regions were identified that resulted in high-quality f (RH)

retrievals. We found that, for CHARMS, the aerosol hygroscopicity is well characterized by a $\kappa_{ext} = 0.27$ ($\kappa_{ext} = 0.31$) at 532 (355) nm, which is comparable to the work from other investigators (Jefferson et al., 2017; Kuang et al., 2017; Zieger et al., 2011). The retrievals compared well to the collocated nephelometers for $\kappa_{ext} < 1$. A unique advantage of the parameterization of lidar f(RH) is the ability to consider multiple profiles to accurately estimate the chemistry-dependent fit parameter κ_{ext} (or γ). We used a matrix algorithm approach to estimate the fit parameters by the lidar where two parameterizations used in the literature were simultaneously implemented. We determined that the f(RH) retrieval by lidar can produce valid results at high time resolution and provide insights on size-dependent hygroscopicity through spectral information. These results could have significant implications on the ability for climate models to more accurately represent aerosol-cloud interactions and the cloud field from f(RH) retrieved near clouds and the top of the mixed layer.

Acknowledgments
This research was supported by the U.S. Department of Energy's Atmospheric System Research, an Office of Science, Office of Biological and Environmental Research program, under Grant DE-SC0016274. Kyle Dawson's research was supported by the NASA Postdoctoral Program at NASA Langley Research Center, administered by Universities Space Research Association under contract with NASA. We thank Rick Wagener, Laurie Gregory, and Lynn Ma for their efforts in establishing and maintaining the SGP AERONET site. We also thank Robert Holz, Willem Marais, and Rob Newsom for collecting the CHARMS data. Finally, we thank John Goldsmith for his work in establishing the ARM Raman lidar. The CHARMS data set is available from the DOE ARM Data Center and IoP archive (https://www.arm.gov/data/data-sources/charms-130).

References

Ackermann, J. (1998). The extinction-to-backscatter ratio of tropospheric aerosol: A numerical study. *Journal of Atmospheric and Oceanic Technology*, *15*(4), 1043–1050. https://doi.org/10.1175/1520-0426(1998)015<1043:TETBRO>2.0.CO;2

Anderson, T. L., Covert, D. S., Marshall, S. F., Laucks, M. L., Charlson, R. J., Waggoner, A. P., et al. (1996). Performance characteristics of a high-sensitivity, three-wavelength, total scatter/backscatter nephelometer. *Journal of Atmospheric and Oceanic Technology*, *13*(5), 967–986. https://doi.org/10.1175/1520-0426(1996)013<0967:PCOAHS>2.0.CO;2

Beaver, M. R., Garland, R. M., Hasenkopf, C. A., Baynard, T., Ravishankara, A. R., & Tolbert, M. A. (2008). A laboratory investigation of the relative humidity dependence of light extinction by organic compounds from lignin combustion. *Environmental Research Letters*, *3*(4), 045003. https://doi.org/10.1088/1748-9326/3/4/045003

Bedoya-Velásquez, A. E., Navas-Guzmán, F., Granados-Muñoz, M. J., Titos, G., Román, R., Casquero-Vera, J. A., et al. (2018). Hygroscopic growth study in the framework of EARLINET during the SLOPE I campaign: Synergy of remote sensing and in situ instrumentation. *Atmospheric Chemistry and Physics*, *18*(10), 7001–7017. https://doi.org/10.5194/acp-18-7001-2018

Beyersdorf, A. J., Ziemba, L. D., Chen, G., Corr, C. A., Crawford, J. H., Diskin, G. S., et al. (2016). The impacts of aerosol loading, composition, and water uptake on aerosol extinction variability in the Baltimore–Washington, D.C. region. *Atmospheric Chemistry and Physics*, *16*(2), 1003–1015. https://doi.org/10.5194/acp-16-1003-2016

Bohren, C. F., & Huffman, D. R. (1998). *Absorption and scattering of light by small particles*. New York, NY: Wiley. https://doi.org/10.1002/9783527618156

Brock, C. A., Wagner, N. L., Anderson, B. E., Attwood, A. R., Beyersdorf, A., Campuzano-Jost, P., et al. (2016). Aerosol optical properties in the southeastern United States in summer—Part 1: Hygroscopic growth. *Atmospheric Chemistry and Physics*, *16*(8), 4987–5007. https://doi.org/10.5194/acp-16-4987-2016

Burgos, M. A., Andrews, E., Titos, G., Alados-Arboledas, L., Baltensperger, U., Day, D., et al. (2019). A global view on the effect of water uptake on aerosol particle light scattering. *Scientific Data*, *6*(1), 157. https://doi.org/10.1038/s41597-019-0158-7

Burton, S. P., Chemyakin, E., Liu, X., Knobelspiesse, K., Stamnes, S., Sawamura, P., et al. (2016). Information content and sensitivity of the $3\beta + 2\alpha$ lidar measurement system for aerosol microphysical retrievals. *Atmospheric Measurement Techniques*, *9*(11), 5555–5574. https://doi.org/10.5194/amt-9-5555-2016

Carrico, C. M. (2003). Mixtures of pollution, dust, sea salt, and volcanic aerosol during ACE-Asia: Radiative properties as a function of relative humidity. *Journal of Geophysical Research*, *108*(D23), 8650. https://doi.org/10.1029/2003JD003405

Chen, J., Li, Z., Lv, M., Wang, Y., Wang, W., Zhang, Y., et al. (2019). Aerosol hygroscopic growth, contributing factors, and impact on haze events in a severely polluted region in northern China. *Atmospheric Chemistry and Physics*, *19*(2), 1327–1342. https://doi.org/10.5194/acp-19-1327-2019

Clegg, S. L., Brimblecombe, P., & Wexler, A. S. (1998). Thermodynamic model of the system $H^+ - NH_4^+ - Na^+ - SO_4^{2-} - NO_3^- - Cl^- - H_2O$ at 298.15 K. *The Journal of Physical Chemistry A*, *102*(12), 2155–2171. https://doi.org/10.1021/jp973043j

Cooper, D. W., Davis, J. W., & Byers, R. L. (1974). Measurements of depolarization by dry and humidified salt aerosols using a lidar analogue. *Journal of Aerosol Science*, *5*(2), 117–123. https://doi.org/10.1016/0021-8502(74)90043-3

Crumeyrolle, S., Chen, G., Ziemba, L., Beyersdorf, A., Thornhill, L., Winstead, E., et al. (2014). Factors that influence surface PM 2.5 values inferred from satellite observations: Perspective gained for the US Baltimore–Washington metropolitan area during DISCOVER-AQ. *Atmospheric Chemistry and Physics*, *14*(4), 2139–2153. https://doi.org/10.5194/acp-14-2139-2014

Davis, K. J., Gamage, N., Hagelberg, C. R., Kiemle, C., Lenschow, D. H., & Sullivan, P. P. (2000). An objective method for deriving atmospheric structure from airborne lidar observations. *Journal of Atmospheric and Oceanic Technology*, *17*(11), 1455–1468. https://doi.org/10.1175/1520-0426(2000)017<1455:AOMFDA>2.0.CO;2

Feingold, G. (2003). Aerosol hygroscopic properties as measured by lidar and comparison with in situ measurements. *Journal of Geophysical Research*, *108*(D11), 4327. https://doi.org/10.1029/2002JD002842

Feltz, W. F., Smith, W. L., Howell, H. B., Knuteson, R. O., Woolf, H., & Revercomb, H. E. (2003). Near-continuous profiling of temperature, moisture, and atmospheric stability using the Atmospheric Emitted Radiance Interferometer (AERI). *Journal of Applied Meteorology*, *42*(5), 584–597. https://doi.org/10.1175/1520-0450(2003)042<0584:NPOTMA>2.0.CO;2

Ferrare, R. A., Melfi, S. H., Whiteman, D. N., Evans, K. D., Poellot, M., & Kaufman, Y. J. (1998). Raman lidar measurements of aerosol extinction and backscattering: 2. Derivation of aerosol real refractive index, single-scattering albedo, and humidification factor using Raman lidar and aircraft size distribution measurements. *Journal of Geophysical Research*, *103*(D16), 19,673–19,689. https://doi.org/10.1029/98JD01647

Gasparini, R., Li, R., Collins, D. R., Ferrare, R. A., & Brackett, V. G. (2006). Application of aerosol hygroscopicity measured at the Atmospheric Radiation Measurement Program's Southern Great Plains site to examine composition and evolution. *Journal of Geophysical Research*, *111*, D05S12. https://doi.org/10.1029/2004JD005448

Goldsmith, J. E. M., Blair, F. H., Bisson, S. E., & Turner, D. D. (1998). Turn-key Raman lidar for profiling atmospheric water vapor, clouds, and aerosols. *Applied Optics*, *37*(21), 4979. https://doi.org/10.1364/AO.37.004979

Granados-Muñoz, M. J., Navas-Guzmán, F., Bravo-Aranda, J. A., Guerrero-Rascado, J. L., Lyamani, H., Valenzuela, A., et al. (2015). Hygroscopic growth of atmospheric aerosol particles based on active remote sensing and radiosounding measurements: Selected cases in southeastern Spain. *Atmospheric Measurement Techniques*, *8*(2), 705–718. https://doi.org/10.5194/amt-8-705-2015

Grund, C. J., & Eloranta, E. W. (1991). University of Wisconsin High Spectral Resolution Lidar. *Optical Engineering*, *30*(1), 6. https://doi.org/10.1117/12.55766

Hänel, G. (1968). The real part of the mean complex refractive index and the mean density of samples of atmospheric aerosol particles. *Tellus*, *20*(3), 371–379. https://doi.org/10.1111/j.2153-3490.1968.tb00378.x

Hänel, G. (1972). Computation of the extinction of visible radiation by atmospheric aerosol particles as a function of the relative humidity, based upon measured properties. *Journal of Aerosol Science*, *3*(5), 377–386. https://doi.org/10.1016/0021-8502(72)90092-4

Hänel, G. (1976). The properties of atmospheric aerosol particles as functions of the relative humidity at thermodynamic equilibrium with the surrounding moist air (pp. 73–188). https://doi.org/10.1016/S0065-2687(08)60142-9

Holben, B. N., Eck, T. F., Slutsker, I., Tanré, D., Buis, J. P., Setzer, A., et al. (1998). AERONET—A federated instrument network and data archive for aerosol characterization. *Remote Sensing of Environment*, *66*(1), 1–16. https://doi.org/10.1016/S0034-4257(98)00031-5

Jefferson, A., Hageman, D., Morrow, H., Mei, F., & Watson, T. (2017). Seven years of aerosol scattering hygroscopic growth measurements from SGP: Factors influencing water uptake. *Journal of Geophysical Research: Atmospheres*, *122*, 9451–9466. https://doi.org/10.1002/2017JD026804

Kasten, F. (1969). Visibility forecast in the phase of pre-condensation. *Tellus*, *21*(5), 631–635. https://doi.org/10.3402/tellusa.v21i5.10112

Kostenidou, E., Pathak, R. K., & Pandis, S. N. (2007). An algorithm for the calculation of secondary organic aerosol density combining AMS and SMPS data. *Aerosol Science and Technology*, *41*(11), 1002–1010. https://doi.org/10.1080/02786820701666270

Kotchenruther, R. A., Hobbs, P. V., & Hegg, D. A. (1999). Humidification factors for atmospheric aerosols off the mid-Atlantic coast of the United States. *Journal of Geophysical Research*, *104*(D2), 2239–2251. https://doi.org/10.1029/98JD01751

Kuang, Y., Zhao, C., Tao, J., Bian, Y., Ma, N., & Zhao, G. (2017). A novel method for deriving the aerosol hygroscopicity parameter based only on measurements from a humidified nephelometer system. *Atmospheric Chemistry and Physics*, *17*(11), 6651–6662. https://doi.org/10.5194/acp-17-6651-2017

Levoni, C., Cervino, M., Guzzi, R., & Torricella, F. (1997). Atmospheric aerosol optical properties: A database of radiative characteristics for different components and classes. *Applied Optics*, *36*(30), 8031. https://doi.org/10.1364/AO.36.008031

Liu, J., & Li, Z. (2018). Significant underestimation in the optically based estimation of the aerosol first indirect effect induced by the aerosol swelling effect. *Geophysical Research Letters*, *45*, 5690–5699. https://doi.org/10.1029/2018GL077679

Liu, Z., Hunt, W., Vaughan, M., Hostetler, C., McGill, M., Powell, K., et al. (2006). Estimating random errors due to shot noise in back-scatter lidar observations. *Applied Optics*, *45*(18), 4437–4447. https://doi.org/10.1364/AO.45.004437

Lv, M., Liu, D., Li, Z., Mao, J., Sun, Y., Wang, Z., et al. (2017). Hygroscopic growth of atmospheric aerosol particles based on lidar, radio-sonde, and in situ measurements: Case studies from the Xinzhou field campaign. *Journal of Quantitative Spectroscopy and Radiative Transfer*, *188*, 60–70. https://doi.org/10.1016/j.jqsrt.2015.12.029

Mattis, I., Ansmann, A., Althausen, D., Jaenisch, V., Wandinger, U., Müller, D., et al. (2002). Relative-humidity profiling in the troposphere with a Raman lidar. *Applied Optics*, *41*(30), 6451–6462. https://doi.org/10.1364/AO.41.006451

Newsom, R. (2012). *Doppler lidar (DL) handbook*. Washington, DC: Department of Energy. https://doi.org/10.2172/1034640

Pahlow, M., Feingold, G., Jefferson, A., Andrews, E., Ogren, J. A., Wang, J., et al. (2006). Comparison between lidar and nephelometer measurements of aerosol hygroscopicity at the Southern Great Plains Atmospheric Radiation Measurement site. *Journal of Geophysical Research*, *111*, D05S15. https://doi.org/10.1029/2004JD005646

Pal, S., Behrendt, A., & Wulfmeyer, V. (2010). Elastic-backscatter-lidar-based characterization of the convective boundary layer and investigation of related statistics. *Annales Geophysicae*, *28*(3), 825–847. https://doi.org/10.5194/angeo-28-825-2010

Parworth, C., Fast, J., Mei, F., Shippert, T., Sivaraman, C., Tilp, A., et al. (2015). Long-term measurements of submicrometer aerosol chemistry at the Southern Great Plains (SGP) using an aerosol chemical speciation monitor (ACSM). *Atmospheric Environment*, *106*, 43–55. https://doi.org/10.1016/j.atmosenv.2015.01.060

Pearson, G., Davies, F., & Collier, C. (2009). An analysis of the performance of the UFAM pulsed Doppler lidar for observing the boundary layer. *Journal of Atmospheric and Oceanic Technology*, *26*(2), 240–250. https://doi.org/10.1175/2008JTECHA1128.1

Petters, M. D., & Kreidenweis, S. M. (2007). A single parameter representation of hygroscopic growth and cloud condensation nucleus activity. *Atmospheric Chemistry and Physics*, *7*(8), 1961–1971. https://doi.org/10.5194/acp-7-1961-2007

Rauber, R. M., Zhao, G., Di Girolamo, L., & Colón-Robles, M. (2013). Aerosol size distribution, particle concentration, and optical property variability near Caribbean trade cumulus clouds: Isolating effects of vertical transport and cloud processing from humidification using aircraft measurements. *Journal of the Atmospheric Sciences*, *70*(10), 3063–3083. https://doi.org/10.1175/JAS-D-12-0105.1

Sisterson, D. L., Peppler, R. A., Cress, T. S., Lamb, P. J., & Turner, D. D. (2016). The ARM Southern Great Plains (SGP) site. *Meteorological Monographs*, *57*, 6.1–6.14. https://doi.org/10.1175/AMSMONOGRAPHS-D-16-0004.1

Thorsen, T. J., & Fu, Q. (2015). Automated retrieval of cloud and aerosol properties from the ARM Raman lidar. Part II: Extinction. *Journal of Atmospheric and Oceanic Technology*, *32*(11), 1999–2023. https://doi.org/10.1175/JTECH-D-14-00178.1

Thorsen, T. J., Fu, Q., Newsom, R. K., Turner, D. D., & Comstock, J. M. (2015). Automated retrieval of cloud and aerosol properties from the ARM Raman lidar. Part I: Feature detection. *Journal of Atmospheric and Oceanic Technology*, *32*(11), 1977–1998. https://doi.org/10.1175/JTECH-D-14-00150.1

Titos, G., Cazorla, A., Zieger, P., Andrews, E., Lyamani, H., Granados-Muñoz, M. J., et al. (2016). Effect of hygroscopic growth on the aerosol light-scattering coefficient: A review of measurements, techniques and error sources. *Atmospheric Environment*, *141*, 494–507. https://doi.org/10.1016/j.atmosenv.2016.07.021

Turner, D. D., Ferrare, R. A., Brasseur, L. A. H., Feltz, W. F., & Tooman, T. P. (2002). Automated retrievals of water vapor and aerosol profiles from an operational Raman lidar. *Journal of Atmospheric and Oceanic Technology*, *19*(1), 37–50. https://doi.org/10.1175/1520-0426(2002)019<0037:AROWVA>2.0.CO;2

Twomey, S. (1977). The influence of pollution on the shortwave albedo of clouds. *Journal of the Atmospheric Sciences*, *34*(7), 1149–1152. https://doi.org/10.1175/1520-0469(1977)034<1149:TIOPOT>2.0.CO;2

Whiteman, D. N., Melfi, S. H., & Ferrare, R. A. (1992). Raman lidar system for the measurement of water vapor and aerosols in the Earth's atmosphere. *Applied Optics*, *31*(16), 3068–3082. https://doi.org/10.1364/AO.31.003068

WMO/GAW. (2016). Aerosol measurement procedures, Guidelines and Recommendation, Report No. 227.

Zieger, P., Fierz-Schmidhauser, R., Poulain, L., Müller, T., Birmili, W., Spindler, G., et al. (2014). Influence of water uptake on the aerosol particle light scattering coefficients of the central European aerosol. *Tellus B: Chemical and Physical Meteorology*, *66*(1), 22,716. https://doi.org/10.3402/tellusb.v66.22716

Zieger, P., Fierz-Schmidhauser, R., Weingartner, E., & Baltensperger, U. (2013). Effects of relative humidity on aerosol light scattering: Results from different European sites. *Atmospheric Chemistry and Physics*, *13*(21), 10,609–10,631. https://doi.org/10.5194/acp-13-10609-2013

Zieger, P., Weingartner, E., Henzing, J., Moerman, M., de Leeuw, G., Mikkilä, J., et al. (2011). Comparison of ambient aerosol extinction coefficients obtained from in-situ, MAX-DOAS and LIDAR measurements at Cabauw. *Atmospheric Chemistry and Physics*, *11*(6), 2603–2624. https://doi.org/10.5194/acp-11-2603-2011

Ziemba, L. D., Lee Thornhill, K., Ferrare, R., Barrick, J., Beyersdorf, A. J., Chen, G., et al. (2013). Airborne observations of aerosol extinction by in situ and remote-sensing techniques: Evaluation of particle hygroscopicity. *Geophysical Research Letters*, *40*, 417–422. https://doi.org/10.1029/2012GL054428